The vibrational distribution of $O_2(X^3\Sigma_g^-)$ produced in the photodissociation of ozone between 226 and 240 and at 266 nm

Joseph D. Geiser[a)]
Department of Chemistry and Chemical Biology, Cornell University, Ithaca, New York 14853

Scott M. Dylewski
School of Applied and Engineering Physics, Cornell University, Ithaca, New York 14853

Julie A. Mueller[b)] and Ruth J. Wilson[c)]
Department of Chemistry and Chemical Biology, Cornell University, Ithaca, New York 14853

Ralf Toumi
Department of Physics, Imperial College, London SW7 2BZ England

Paul L. Houston[d)]
Department of Chemistry and Chemical Biology, Cornell University, Ithaca, New York 14853

(Received 2 August 1999; accepted 20 October 1999)

Resonance-enhanced multiphoton ionization coupled with time-of-flight product imaging has been used to study the $O_3(X\,^1A_1)+h\nu\rightarrow O(2p\,^3P_J)+O_2(X\,^3\Sigma_g^-)$ product channel in the UV (ultraviolet) photodissociation of ozone at photolysis wavelengths of 226, 230, 233, 234, 240, and 266 nm. These imaging experiments, together with a measurement of the branching ratio into the different spin orbit states of the O atom, allowed the determination of the yields of the O_2 product in vibrational states greater than or equal to 26 as a function of wavelength. It was found that at 226, 230, 233, 234, and 240 nm, the yield was $11.8\pm1.9\%$, $11.5\pm1.2\%$, $8.2\pm2.0\%$, $4.7\pm1.8\%$, and $0.6\pm0.1\%$, respectively. © *2000 American Institute of Physics.* [S0021-9606(00)01203-4]

INTRODUCTION

The Hartley band of ozone is a broad absorption feature from about 200–310 nm consisting of a continuum with some structure superimposed on it. Upon absorption, the molecule dissociates, predominantly following the spin-allowed channels

$$O_3(X\,^1A_1)+h\nu\rightarrow O(^1D_2)+O_2(a\,^1\Delta_g) \tag{1}$$

and

$$O_3(X\,^1A_1)+h\nu\rightarrow O(^3P_J)+O_2(X\,^3\Sigma_g^-). \tag{2}$$

The singlet channel is the dominant of these two channels with a yield of 85%–90%. Interestingly, the minor triplet channel yields oxygen molecules with a bimodal energy distribution with a significant fraction of the molecules formed in very high vibrational states.[1] The cause for this vibrational bimodality is not known. The possibility that the high vibrational excitation comes from elimination of the central oxygen atom with recombination of the end atoms to form the O_2 product is appealing, but the angular distributions of the products suggest that this is not a likely mechanism.[2] The $O(^3P_J)$ atoms produced in coincidence with both the $O_2(v\geqslant 26)$ and $O_2(v<26)$ have similar high and positive anisotropy parameters, whereas elimination of the central atom, at least along a C_{2v} path, would produce a negative anisotropy parameter. A more likely explanation for the bimodality might be that there are multiple regions where the dissociative triplet surface leading to the $O(^3P_J)+O_2(^3\Sigma_g^-)$ products crosses the bound excited surface, which correlates with $O(^1D)+O_2(^1\Delta_g)$.[2] Another possible explanation is that there is more than one excited state responsible for the absorption. In order to evaluate these possibilities, it is necessary to know how the yield of the $O_2(^3\Sigma_g^-, v\geqslant 26)$ product varies with wavelength.

In addition to the fundamental interest in understanding the dynamics of this photodissociation, it is important to understand the quantity and fate of the vibrationally excited oxygen molecules generated from ozone in the stratosphere. Even though only 10%–15% of the photodissociation events follow this minor channel, a relatively large amount of vibrationally excited O_2 may be generated because the cycle of $O+O_2$ recombination and ozone dissociation occurs more than 50 times, depending on altitude, for every ozone formed by photodissociation of O_2 or lost by catalytic decomposition.

Previous studies have suggested that this energetic oxygen might be implicated in a solution to the well-studied ozone deficit problem.[3,4] In the upper stratosphere and the mesosphere, that is, at altitudes from about 35–80 km, ozone is in a photochemical steady state. The ozone abundance in this region of the atmosphere is thought to be controlled by a relatively small number of chemical reactions, each of which is well characterized. Therefore, ozone concentrations should

a)Current address: Department of Chemistry, University of New Hampshire, Parsons Hall, Durham, NH 03824.
b)Current address: The James Franck Institute, 5640 S. Ellis Ave., Chicago, IL 60637.
c)Current address: Engineering and Physical Sciences Research Council, Polaris House, North Star Avenue, Swindon, Wiltshire, SN2 1ET England.
d)Electronic mail: plh2@cornell.edu

be amenable to model simulations. However, this apparently straightforward calculation has given rise to a long standing and puzzling problem in stratospheric ozone chemistry, the so called ''ozone deficit.'' The deficit refers to the mismatch between measured stratospheric ozone concentrations and modeled ones, both as functions of altitude. The modeled values appeared to generally fall lower than the observed quantities, so there seemed to be a deficit in our understanding of ozone chemistry. The actual magnitude and significance of the deficit is a matter of some debate.[5–12] Recent use of O_3 observations that appear to be more accurate than those used previously suggest is that there is no need to question the standard models.[10–12]

Even if a deficit exists, it now seems unlikely that the previously proposed new ozone source based on the vibrationally excited O_2 is valid. The proposed additional ozone-producing mechanism is given by the following scheme:[13]

$$O_3 + h\nu(\lambda < 243\ \text{nm}) \rightarrow O_2(X\,^3\Sigma_g^-, v \geqslant 26) + O(^3P_J), \tag{3}$$

$$O_2(X\,^3\Sigma_g^-, v \geqslant 26) + O_2(X\,^3\Sigma_g^-, v = 0) \rightarrow O_3(X\,^1A_1) + O(^3P_J), \tag{4}$$

$$2 \times \{O(^3P_J) + O_2(X\,^3\Sigma_g^-) + M \rightarrow O_3 + M\}. \tag{5}$$

$$\text{Net:} \quad 3O_2(X\,^3\Sigma_g^-) + h\nu \rightarrow 2O_3$$

Although several recent experimental studies on the UV photodissociation of ozone have confirmed that $O_2(^3\Sigma_g^-, v \geqslant 26)$ is produced in the dissociation of ozone,[1,14–20] there is no direct experimental evidence for the occurrence of reaction (4). The stimulated emission pumping (SEP) experiments performed by the Wodtke group[13–21] indicated that at 295 K there is a large increase in the rate for $O_2(v)$ disappearance when v increases from 25 to 26. Reaction (4) was implicated because the energy at which this rate increase occurs corresponds to its thermodynamic threshold, and further relaxation experiments tended to support this view. However, several groups have now studied theoretically either the reverse of reaction (4)[22–27] or reaction (4) in the forward direction,[25,26,28–34] and none have found evidence for the reaction using either the semiempirical Varandas–Pais potential[25,26,29,31–34] or *ab initio* surfaces.[28,30]

Regardless of whether or not the vibrationally excited $O_2(^3\Sigma_g^-)$ product is involved in ozone production, it is important to characterize its production rates in the stratosphere and to understand the dynamics of its formation. We have thus proceeded to determine the yield of $O_2(v \geqslant 26)$ as a function of ozone dissociation wavelength. The technique of time-of-flight product-imaging has been utilized to determine the yield of $O_2(X\,^3\Sigma_g^-, v \geqslant 26)$ at five ozone photolysis wavelengths between 226 and 240 nm. The experimental procedure and subsequent analysis of the data are very similar to that performed by Miller *et al.*[1] for ozone dissociation at 226 nm. We have repeated the measurement at 226 nm since improvements have been made to our experimental technique that substantially increase the velocity resolution.

EXPERIMENT

The product imaging experimental details have been described more fully elsewhere.[2,35] A molecular beam of ozone was formed by flowing helium with about 810 Torr backing pressure over ozone maintained on silica gel at a temperature of $-78\,^\circ$C. The subsequent mixture of $<1\%$ ozone was expanded through a pulsed 250 μm diam nozzle and collimated by a 500 μm diam skimmer mounted about 5 mm from the nozzle orifice. Further downstream, the molecular beam was crossed at right angles by two counter-propagating laser beams, one serving to dissociate the ozone and the other to probe the resulting $O(^3P_J)$ fragments using the $O(3p\,^3P_{2,1,0} \leftarrow\leftarrow 2p\,^3P_J)2+1$ REMPI (resonantly enhanced multiphoton ionization) scheme at 226.23, 226.06, and 225.65 nm for $J=0$, 1, and 2, respectively.[36,37] Due to the large Doppler width of the $O(^3P_J)$ fragments it was necessary to scan the probe laser over the resonance to ensure that the images detect all product $O(^3P_J)$ atom velocities with equal sensitivity.

The dissociating laser radiation between 230 and 266 nm was produced by frequency doubling the output of an optical parametric oscillator (Spectra-Physics MOPO-730) pumped by an injection seeded Nd:YAG laser (Spectra Physics GCR-230). Typical laser powers were 1–3 mJ/pulse with a pulse duration of 8–10 ns. The tunable light needed to probe the $O(^3P_J)$ fragments at 226 nm was generated by frequency doubling the output of an injection-seeded, Nd:YAG-pumped dye laser and then summing the doubled light with the Nd:YAG laser fundamental; typical powers achieved were 1.0 mJ/pulse with a pulse duration of 8–10 ns. Both lasers were operated at 10 Hz. For studies of photodissociation at 226 nm, the laser at this wavelength served as both the photolysis and the probe laser. Photolysis and probe beams were directed into the vacuum chamber and focused into the interaction region by 25 and 7.5 cm focal length plano-convex lenses, respectively. The polarizations of both the photolysis and probe laser beams were perpendicular to the plane defined by the molecular and laser beams.

The velocity mapping-ion counting technique[35,38] was used to obtain high-resolution photofragment images. An electrostatic lens was employed that served both to extract the ionized $O(^3P_J)$ fragments from the interaction zone and to de-blur the image. The magnification factor of this electrostatic lens was measured to be 1.17 ± 0.02 by dissociating O_2 and detecting the oxygen atom fragment with the same REMPI scheme used in the ozone experiments. The ionized fragments were accelerated into a flight tube mounted along the axis of the molecular beam. The ions were imaged by a position sensitive detector consisting of a chevron double micro-channel plate (MCP) assembly coupled to a fast phosphor screen. The image on the phosphor screen was recorded by a 640×480 pixel charge coupled device (CCD) camera. Both the MCP and CCD camera were electronically shuttered to collect signal corresponding to the mass of the oxygen atoms. Signal levels were kept below 200 ions per shot to avoid saturation of the MCP for images with bright central features. Data were accumulated typically for 100 000 total laser shots.

One experimental complication is the potential ''con-

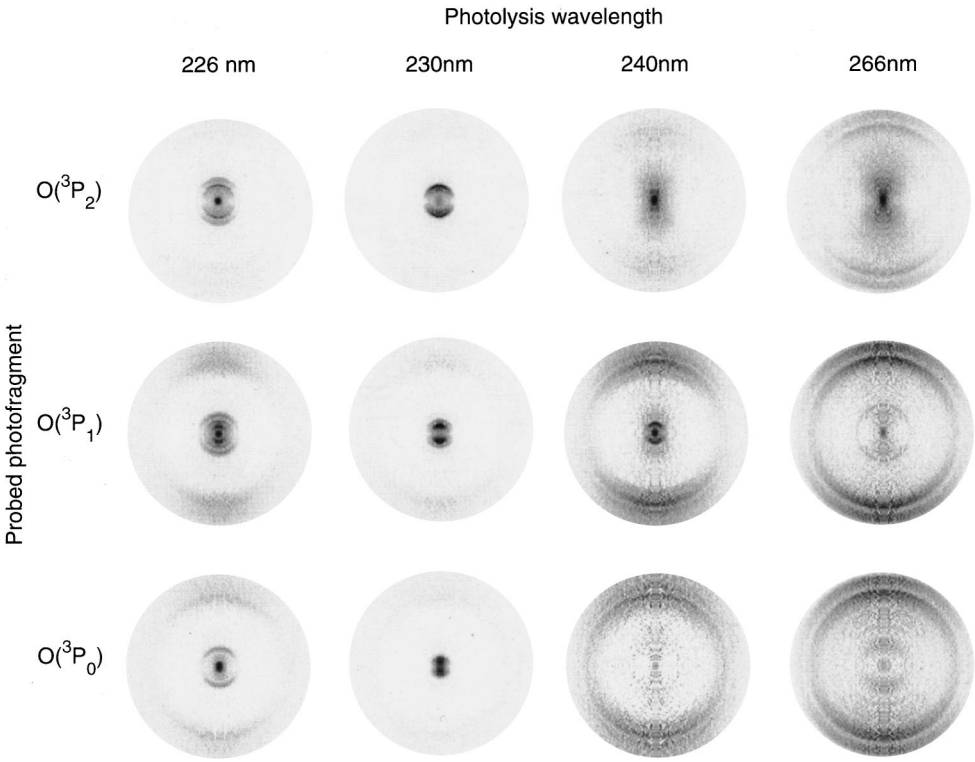

FIG. 1. Table of the reconstructed 3D distributions of the $O(^3P_J)$ fragments from ozone photodissociated at 226, 230, 240, and 266 nm.

tamination'' of the images obtained in two-color experiments by signal due to dissociation by the 226 nm probe radiation. Careful adjustment of both the spatial and temporal overlap between the two laser pulses, coupled with the high power of the photolysis pulse and low ozone concentration in the molecular beam allowed images to be acquired with minimal probe contamination. In spite of these precautions, some of the images with photolysis wavelengths between 230 and 240 nm were contaminated with one-color 226 nm signal. This signal was removed by subtracting an appropriately scaled amount of pure 226 nm signal from the image. A much smaller source of background contamination was also present due to the one-color signal from 230 to 240 nm radiation. Images of these background signals were collected and their contribution was subtracted from the two-color product images. The resulting data is a two-dimensional projection of the $O(^3P_J)$ photofragment's three-dimensional velocity distribution. Because the projection is made perpendicular to the electric vectors of the dissociation and probe radiation, it is possible to reconstruct the original three-dimensional velocity distribution using the inverse Abel transform.[39–41]

The branching ratios for the fine structure states of the $O(^3P_J)$ were measured by placing a 2 in. diam active area photomultiplier tube (Thorn EMI 9235QB) near the phosphor screen to collect all of the ion signal as the probe laser was tuned over the $O(^3P_J)$ Doppler profile at laser wavelengths of 226.23, 226.06 and 225.65 nm for $j=0$, 1, and 2, respectively. The output of the photomultiplier was sent to a boxcar averager gated at the appropriate arrival time. The probe laser power was simultaneously measured with a photodiode in order to normalize the $O(^3P_J)$ signal intensity for fluctuations in laser power.

RESULTS

Our experimental efforts have concentrated on the $O(^3P_J)$ fragments formed in the minor photodissociation channel of ozone, probed through a $2+1$ REMPI scheme, at six photolysis wavelengths between 226 and 266 nm. The images shown in Fig. 1 are slices through the reconstructed three-dimensional distributions of the $O(^3P_J)$ fragments at four of these wavelengths. The electric vector of the dissociating light is parallel to the vertical direction in the plane of the image. The images have been altered slightly to correct for the inverse Abel transform singularity along the vertical axis by fitting the angular distributions to a $A[1+\beta P_2(\cos\theta)]$ distribution and interpolating across the middle 12 pixels for radii greater than 10 pixels. The recovered $O(^3P_J)$ velocity distributions from the inverse Abel transformed slices can be separated into angular and speed components. Angular distributions are determined by integrating over the desired speed interval for each angle.[2] Extraction of the speed distribution is achieved in an analogous manner by integrating over all angles for each speed. The speed distributions can be further transformed, using the law of conservation of momentum, into total translational energy distributions for the $O_3 \rightarrow O_2(X\,^3\Sigma_g^-) + O(^3P_J)$ dissociation.

From pump–probe experiments detecting the LIF (laser induced fluorescence) signal from $O_2(X\,^3\Sigma_g^-, v=26)$, it is known that the imaged oxygen atoms are paired with ground electronic state O_2 molecules.[1] The vibrational distribution of the O_2 product can, therefore, be determined by imaging the atomic fragment and using conservation of energy,

$$KE = E_{h\nu} - D_0(\mathrm{O_2{-}O}) - T_{\mathrm{O_2}}(v) + \mathrm{ZPE}_{\mathrm{O_2}} - F_{v\mathrm{O_2}}(J) - E_{\mathrm{O}(3Pj)}, \quad (6)$$

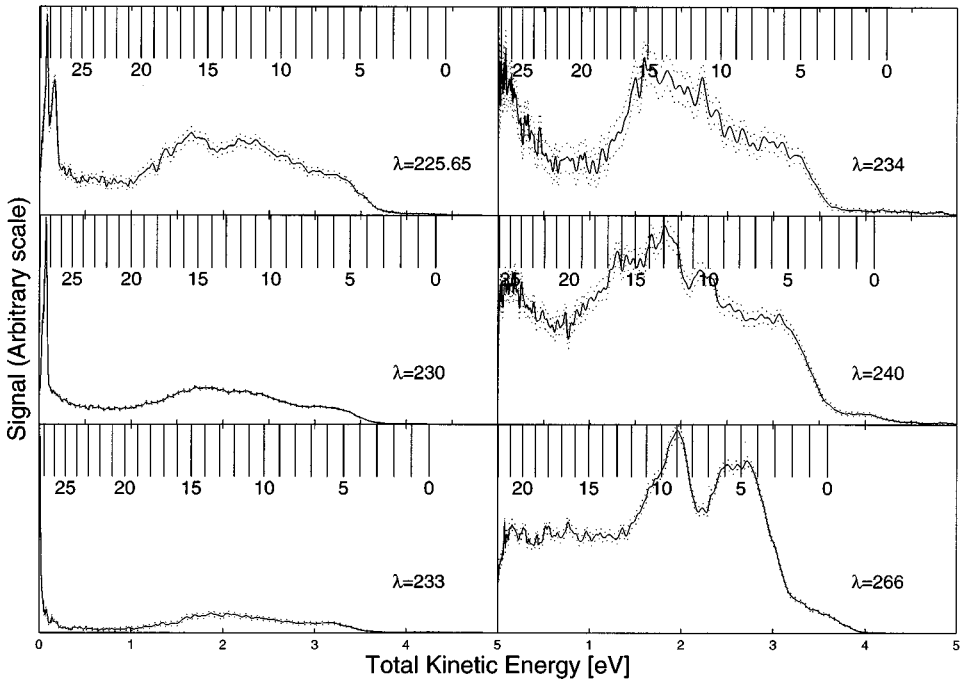

FIG. 2. The total translational energy distributions for the dissociation of O_3 to $O(^3P_2)+O_2(X\,^3\Sigma_g^-)$ at 226, 230, 233, 234, 240, and 266 nm. The vibrational levels of the $O_2(X\,^3\Sigma_g^-, J=0)$ fragment are indicated by the combs. The dotted curves represent the uncertainty in the signal intensity arising from counting statistics. Similar data, though differing in the details of the distribution, were obtained for the $O(^3P_1)$ and $O(^3P_0)$ fragments.

where $D_0(O_2-O)$ is the ozone dissociation of energy 1.0523 ± 0.0026 eV,[42] $T_{O_2}(v)$ is the vibrational term, $F_{v,O_2}(J)$ the rotational term calculated from the spectroscopic constants given by Laher and Gilmore,[43] ZPE_{O_2} is the zero-point energy of the O_2 fragment, and $E_{O(3PJ)}$ are the $O(^3P_J)$ energies obtained from Moore's table.[44] The energy distributions together with a comb indicating the energy of the vibrational states of the O_2 fragment formed in conjunction with $O(^3P_2)$ are shown in Fig. 2. It is interesting to note that virtually all of the oxygen molecules formed are vibrationally excited. The population of interest for the ozone deficit problem is that in $v\geqslant 26$. This population is determined from the images for each spin–orbit state as a function of wavelength and is shown in Table I. The uncertainties reported in Table I take several factors into account. Uncertainty in the intensity of the image arises from counting statistics and from variation in the detector's efficiency in its different quadrants. There is uncertainty in the energy axis arising from uncertainty in the magnification factor and the flight time.

The branching ratios into the various $O(^3P_J)$ states were surprisingly difficult to measure. The power dependence of the ionizing laser at the center of the Doppler profile was measured before each scan of the Doppler profile to provide proper normalization of the power dependence. It was found that the combination of our laser power and sample concentration put us on an inconvenient place on the saturation curve, leading to dependencies ranging from quadratic to cubic. The laser power was measured during the scans, and the resulting profile was normalized for variations in this power. The data was also normalized by the two-photon line strength,[37] but this correction was small. The results are shown in Table II. The reported uncertainties represent 2σ of 9, 4, 3, and 3 measurements at 226, 230, 240, and 266 nm, respectively.

The total fraction of $O_2(v\geqslant 26)$ generated from the photodissociation of ozone at a particular wavelength is given by

TABLE I. The percent population of O_2 from the triplet channel in $v\geqslant 26$ as a function of photolysis wavelength and spin–orbit state of the counter fragment. Note that the thermodynamic threshold for the generation of $O_2(v=26)$ is at 241.6 nm.

	226 nm	230 nm	233 nm	234 nm	240 nm
$O(^3P_2)$	14.5 ± 2.0	16.8 ± 3.8	15.2 ± 0.2	6.9 ± 0.9	0.70 ± 0.10
	11 ± 3[a]				
$O(^3P_1)$	5.5 ± 0.5	5.1 ± 0.7	0.7 ± 0.2	0.8 ± 0.2	0.30 ± 0.10
	5.9 ± 2.0[a]				
$O(^3P_0)$	3.6 ± 0.5	4.1 ± 0.6	0.4 ± 0.2	0.6 ± 0.2	0.10 ± 0.05
	4.6 ± 2.0[a]				

[a]Reference 15.

TABLE II. The branching ratios into the three spin–orbit states of the oxygen atom fragment as a function of photolysis wavelength in the Hartley band. Note that a statistical yield would give a branching ratio of 5:3:1, or as percentages, 55.5:33.3:11.1.

	$O(^3P_2)$	$O(^3P_1)$	$O(^3P_0)$	
226 nm	69 ± 9	23 ± 3	7.7 ± 2.2	this work
	45	39	16	[a]
	59 ± 4	30 ± 2	11	[b]
	55	35	15	[c]
	45 ± 10	36 ± 10	18 ± 10	[d]
230 nm	55 ± 3	31 ± 4	14 ± 2	this work
240 nm	67 ± 5	25 ± 5	7.9 ± 0.4	this work
266 nm	66 ± 3	26 ± 1	8.5 ± 2.6	this work
	55 ± 3	23 ± 3	12 ± 3	[e]
308 nm	66 ± 3	27 ± 3	9 ± 1	[e]

[a]Reference 46.
[b]Reference 1.
[c]Reference 14.
[d]Reference 15.
[e]Reference 52.

TABLE III. The total percentage of minor channel product created in $v \geqslant 26$ as a function of photolysis wavelength.

Wavelength (nm)	Percent population in $v \geqslant 26$	Assuming statistical
226	11.8±1.9	10.3
230	11.5±1.2	11.5
233	···	8.2
234	···	4.7
240	0.6±0.1	0.5

$$F_{v\geqslant 26}(\lambda) = F_t(\lambda) R_{v>26}(\lambda), \tag{7}$$

where $F_t(\lambda)$ is quantum yield of triplet channel and $R_{v>26}(\lambda)$ is fraction of triplet channel product formed in $v \geqslant 26$ at that same wavelength. The photofragment product imaging data combined with the measured branching ratios allows the determination of the latter value as

$$R_{v\geqslant 26}(\lambda) = \frac{\Sigma_J F_{3PJ}(\lambda) F_{J,v\geqslant 26}(\lambda)}{\Sigma_J F_{3PJ}(\lambda)}, \tag{8}$$

where $F_J,\ v\geqslant 26(\lambda)$ is the fraction of O_2 formed in coincidence with $O(^3P_J)$ that is in $v \geqslant 26$, shown in Table I, and $F_{3PJ}(\lambda)$ is the branching ratio of minor channel product into $O(^3P_J)$, shown in Table II. The branching ratio was not measured for 233 and 234 nm dissociation. At these wavelengths a statistical population was assumed with estimated uncertainties of 10%, 6%, and 3% in the $J=2$, 1, and 0 state, respectively. The resulting populations are summarized in Table III and plotted in Fig. 3.

The imaging data also provides angular information. The measured angular distributions at 226, 230, 240, and 266 nm agree qualitatively with those measured earlier in our laboratory.[2] In this previous work, both the 226 and 230 nm images showed a slightly lower anisotropy parameter β at low velocities than in the data presented here. This result is consistent with the observation that the previous images were affected by saturation of the central feature on the MCP. Note that the β values for very high velocities are likely to be incorrect because there are **v-J** correlations for the $O(^3P_1)$ and $O(^3P_2)$ velocities.

DISCUSSION

The velocity mapping-ion counting technique increases the resolution of imaging data. This is clearly seen when it is compared with the data from the conventional Wiley–McLaren imaging apparatus[1] or even the more recent data employing solely the velocity mapping technique.[38] This improvement allowed the observation of previously unresolved structure in all the photolysis images collected here. This structure spans multiple vibrational levels and is indicative that a complicated photodissociation dynamics occurs in this three atom system.

A further quantitative improvement over the previous imaging work was due to the discovery that the intense central feature of many of the images was saturating the position sensitive MCP, but only in those locations with high ion flux. Thus the relative intensities of faster fragments (lower vibrational energy in the O_2 fragment) were artificially augmented in previous work.[1,2]

Takahashi *et al.*[45] have reported a measurement of the translational energy distribution for the $O(^3P_J)$ fragment from 266 nm photodissociation of ozone. The atomic fragment was detected using VUV-LIF (vacuum ultraviolet-laser induced fluorescence). Although the resolution of this data is extremely low, it agrees qualitatively with that reported here, except for the strong minimum observed in their data at about 0.8 eV. We are unaware of any other measurements of the $O(^3P_J)+O_2(^3\Sigma)$ translational energy distributions at wavelengths of 230–240 nm.

Our measurements of the branching ratios are significantly different than many of those obtained in other laboratories. These data are shown in Table II. There seems to be a wide range of scatter in the different measurements at 226

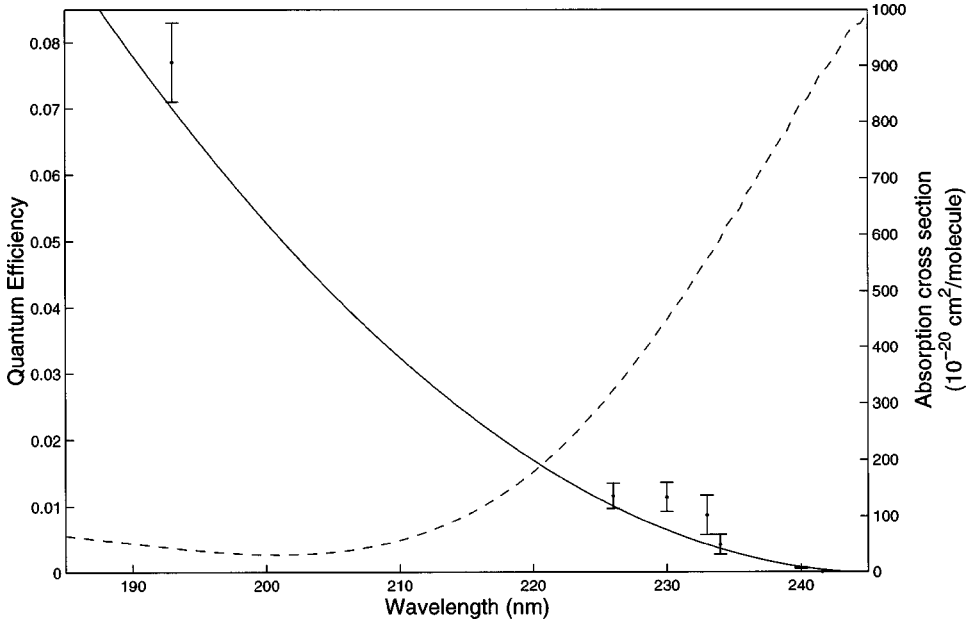

FIG. 3. Plot of the quantum efficiency for the formation of $O_2(v\geqslant 26)$ as a function of wavelength. The value at 193 nm is taken from Stranges *et al.* (Ref. 17). A 10% branching ratio into the triplet channel is assumed. The absorption cross section taken from Molina and Molina (Ref. 51) for ozone is plotted as the dashed curve on the right hand axis.

TABLE IV. The ozone photodissociation wavelength in nm corresponding to the energetic threshold for the formation of vibrationally excited O_2 with $O(^3P_J)$ based on the recent measurement of Jongma *et al.* (Ref. 53).

	$O_2(v=26)$	$O_2(v=27)$	$O_2(v=28)$	$O_2(v=29)$	$O_2(v=30)$	$O_2(v=31)$
$O(^3P_2)$	241.6	236.3	231.4	226.9	222.8	219.0
$O(^3P_1)$	240.7	235.4	230.6	226.1	222.0	218.2
$O(^3O_0)$	240.3	235.0	230.2	225.8	221.7	217.9

nm, and none of them quite agrees with our values; for example, every measurement finds less $O(^3P_2)$ than we do. The closest value to ours is the measurement that was previously performed by this group. Also at 266 nm we find more population in $O(^3P_2)$ than the other measurement. Our values are fairly constant at all four wavelengths and agree more closely with the literature values at 308 nm, the exception being at 230 nm, where we found an essentially statistical distribution. It seems likely that our values are high. One possible contribution to this would be the presence of thermal oxygen atoms from the decomposition of ozone on the metal surfaces of the sample line.

The goal of these experiments was to measure the fraction of $O_2(v\geqslant 26)$ formed in the triplet channel. Our results are shown in Table III. Given the concern with the measured branching ratios into the different spin–orbit states of $O(^3P)$, we might ask how dependent these values are on the exact branching ratios used. The final column shows the fraction of $O_2(v\geqslant 26)$ calculated if a statistical distribution is assumed. These two sets of values represent what seems to be the two extremes of the branching ratio. The resulting fractions of $O_2(v\geqslant 26)$ formed are not significantly different.

Previous measurements of the fraction of $O_2(v\geqslant 26)$ formed in the minor channel for photodissociation at 226 nm were consistently lower than our current value, although they agree closely with each other. Miller *et al.*[1] measured 8.1% while Syage[16] found $7.9\%\pm 2.0\%$ in $v\geqslant 26$. The results should be higher than the previous imaging measurement[1] because of the saturation effect discussed above, in which the relative intensities of slower fragments (higher vibrational energy in the O_2 fragment) were artificially suppressed. Although our new measurement is not as close to that of Syage as the previous measurement, the new value is still within the error limit. Kinugawa *et al.*[46] show a translational energy distribution for the $O(^3P_1)$ fragment that agrees qualitatively with our data. However, their data seem to have more intensity in the lowest vibrational levels $(v=0-3)$.

One motivation for these particular experiments was to be able to evaluate possible implications for the ozone deficit problem. If a deficit exists and if $O_2(^3\Sigma_g^-, v\geqslant 26)$ leads to formation of two ozone molecules, then accurate values for the amount of vibrationally excited O_2 formed as a function of wavelength would be needed for proper modeling. Previous data on the yield of $O_2(v\geqslant 26)$ were available only at 193 and 226 nm, and models assumed a yield as a function of wavelength that passed through these points and the energetic threshold for $O_2(v=26)$ at 241.6 nm. The experiments reported here have added several points to the high wavelength end of this region. It is particularly important to characterize the yield in this wavelength region because the ozone absorption cross section increases rapidly with wavelength as shown in Fig. 3. The wavelength dependence of the yield is tied to the altitude dependence of ozone concentration because the solar flux changes significantly with altitude; see, e.g., Ref. 47.

The points in Fig. 3 give the wavelength dependence of the $O_2(v\geqslant 26)$ yield. Also shown is the original fit by Toumi *et al.* using only data at 193, 226, and 243 nm.[18]

$$Q=1.493\,88-0.012\,125\lambda+2.4599\times 10^{-15}\lambda^2. \tag{9}$$

Although the fit does not capture the onset of $O_2(v\geqslant 26)$ near 234 nm, it does about as well as can be done using a quadratic polynomial.

Given the current state of the theoretical work on reaction (4), the model calculation[18] represents an upper limit for ozone production because it assumes that all of the $O_2(v\geqslant 26)$ reacts to form ozone. Even if reaction (4) occurs, it is unlikely that all of the excited oxygen molecules follow this reaction. The dependence of the $O_2(v\geqslant 26)$ yield on wavelength shown by the points in Fig. 3 is similar enough to that assumed previously that it appears likely that the new measurements will not change the previous results. We thus again come to the conclusion that, if there is a mechanism for generating ozone from the vibrationally excited O_2, then the production yield of $O_2(v\geqslant 26)$ from ozone photolysis partially accounts for the ozone deficit problem, particularly at the lowest altitudes at which the problem is manifest. It does not account for the ozone deficit at higher altitudes.

Although it should eventually be possible to explain much of the structure in each of the individual images, more theoretical effort is first needed concerning the nature of the electronic states of ozone reached by these dissociation wavelengths. A few conclusions can nonetheless be made. First, the two regions in the bimodal distribution seen in the lower wavelength images arise from distinct processes. This is seen clearly by examining the angular distributions. For the slower fragments, there is a well defined β value, while for the fast fragments a **v-J** correlation becomes pronounced, leading to a different yet less well defined β value.[2] This observation is strong evidence that two different processes lead to these products.

Second, there appears to be a distinct threshold for forming $O_2(v\geqslant 26)$. The photodissociation wavelengths corresponding to the energetic thresholds for forming $O_2(v)$ in association with the three spin–orbit states of the atomic product are shown in Table IV. The highly excited fragments begin to be observed near 234.5 nm, a wavelength that corresponds to the formation rotationally excited molecules in $v=27$. This is also clearly seen from the vibrational combs in Fig. 2.

Third, there are clear differences in the images for dissociation at the same wavelength while probing different spin–orbit states. Two effects contribute to these differences. One is the slight difference in energy in the atomic states, most easily seen in the data at 234 nm where the $O(^3P_2)$ data clearly has the strong contribution from vibrationally excited O_2 while the other spin–orbit states do not. In this case the threshold for the dynamical process that forms the vibrationally excited products has been crossed by the 158.265 cm^{-1} of the spin–orbit excitation. The second effect is that due to the nature of the *J*-level. It is known that there is a **v-J** correlation from the angular fits as well as from the fact that when the polarization of the probe laser is rotated 90°, the image changes. The extent of this correlation can be different for different values of *J*. This is most evident for the case where $J=0$, as in this instance there is no **v-J** correlation.

The bimodal feature in the lower wavelength images is accounted for by the presence of the two processes for which evidence has been presented above. There is also a clear bimodality in the data from 266 nm dissociation. The energy distribution displays peaks at 2.7 and 3.6 eV. This distribution raises further questions since the process creating $O_2(v\geqslant 26)$ at lower wavelengths is no longer energetically accessible. One possibility is that it arises from a previously unobserved spin-forbidden process in the Hartley band. Energetically, the lower energy feature corresponds to the channel.

$$O_3+h\nu\rightarrow O(^3P)+O_2(b\,^1\Sigma_g^+).$$

This channel has recently been observed in the 335–352 nm region of the Huggins band.[48] Such a channel is not inconsistent with previously determined branching ratios in the Hartley band. These determinations typically rely on measuring the amount of $O(^3P)$ as a function of time and inferring the channels present from the observed kinetics. Such a measurement accounts for the amount of $O(^1D)$ versus $O(^3P)$ formed but not which channels gives rise to these species.

We cannot say that the low energy feature is indeed due to this spin-forbidden channel without further corroboration, that is, direct measurement of the $O_2(b\,^1\Sigma_g^+)$ product, for example by a $2+1$ REMPI process.[49] Such work is currently underway in our laboratory. There are several complications in this measurement. First, only one rovibrational state of the $O_2(b\,^1\Sigma_g^+)$ may be probed at a time. Thus, if this spin-forbidden process occurs, the amount of signal is dependent upon the nascent rovibrational distribution. Second, $O(^1D)$ readily reacts with $O_2(X\,^3\Sigma_g^-)$ to form $O_2(b\,^1\Sigma_g^+)$.[50] Because $O(^1D)$ is readily formed in the UV photodissociation of ozone, this reaction is likely to give a significant background signal. However, if this channel does occur, it is pertinent to ask what its wavelength dependence might be. It is interesting to note that the images at other wavelengths have peaks or shoulders at the energetic threshold for this spin-forbidden channel.

CONCLUSIONS

Product imaging has provided detailed information on the vibrational distribution of $O_2(^3\Sigma_g^-)$ produced in the dissociation of ozone at wavelengths between 226 and 240 nm and at 266 nm. The distributions for wavelengths of 233 nm and below are bimodal, with one peak in the distribution near $v=14$ and another near $v=27$. At wavelengths of 235 nm or longer, the peak at the $v=27$ disappears. When combined with a measurement of the branching ratio to different spin–orbit states of the $O(^3P_J)$ atom, it is possible to determine the fraction of $O_2(^3\Sigma_g^-)$ produced in levels $v\geqslant 26$ as a function of wavelength. The wavelength dependence of this fraction is similar to that used previously to calculate the effect of $O_2(^3\Sigma_g^-, v\geqslant 26)$ on the production rate of ozone, so that we do not expect the conclusion to be different: If there is an ozone deficit production of $O_2(^3\Sigma_g, v\geqslant 26)$ may account for the ozone deficit near 40 km, but cannot account for the deficit at higher altitudes, even if all the $O_2(^3\Sigma_g^-, v\geqslant 26)$ leads to production of ozone via a reaction similar to Eq. (4).

The vibrational distribution of the $O_2(^3\Sigma_g^-)$ and the angular distributions of individual parts of this distribution indicate that there is more than one dissociation mechanism for production of $O_2(^3\Sigma_g^-)$. Additional hints about the dissociation mechanism are provided by the sharp onset with decreasing wavelength of the $O_2(^3\Sigma_g^-, v\geqslant 26)$ yield and by the variation in the vibrational distribution of $O_2(^3\Sigma_g^-)$ with the spin–orbit state of the sibling $O(^3P_J)$.

ACKNOWLEDGMENTS

This work has been supported by the National Science Foundation under Grant No. ATM-9528086 and by the Research Institute of Innovative Technology for the Earth administered by the New Energy and Industrial Technology Development Organization of Japan. We are grateful to Dr. Bor-Yu Chang for experimental help and for lively discussions.

[1] R. L. Miller, A. G. Suits, P. L. Houston, R. Toumi, J. A. Mack, and A. M. Wodtke, Science **265**, 1831 (1994).
[2] R. J. Wilson, J. A. Mueller, and P. L. Houston, J. Phys. Chem. A **101**, 7593 (1997).
[3] R. Toumi, B. J. Kerridge, and J. A. Pyle, Nature (London) **351**, 217 (1991).
[4] J. Eluskiewicz and M. Allen, J. Geophys. Res. **98**, 1069 (1993).
[5] T. G. Slanger, Science **265**, 1817 (1994).
[6] D. E. Siskind, B. J. Connor, R. S. Eckman, E. E. Remsberg, J. J. Tsou, and A. Parrish, J. Geophys. Res. **100**, 11191 (1995).
[7] A. E. Dessler, S. R. Kawa, D. B. Considine, J. W. Waters, L. Froidevaux, and J. B. Krumer, Geophys. Res. Lett. **23**, 339 (1996).
[8] K. W. Jucks, D. G. Johnson, K. V. Chance, W. A. Traub, R. J. Salawitch, and R. A. Stachnik, J. Geophys. Res. **101**, 28785 (1996).
[9] P. Crutzen, Science **277**, 1951 (1997).
[10] M. B. McElroy and R. J. Salawitch, Planet. Space Sci. **37**, 1653 (1989).
[11] M. Natarajan and L. B. Callis, Geophys. Res. Lett. **16**, 473 (1989).
[12] P. J. Crutzen, J.-U. Grooβ, C. Brühl, R. Müller, and J. M. Russell III, Science **268**, 705 (1995).
[13] J. M. Price, J. A. Mack, C. A. Rogaski, and A. M. Wodtke, Chem. Phys. **175**, 83 (1993).
[14] J. A. Syage, J. Phys. Chem. **99**, 16530 (1995).
[15] J. A. Syage, J. Chem. Phys. **105**, 1007 (1996).
[16] J. A. Syage, J. Phys. Chem. **100**, 13885 (1996).
[17] D. Stranges, X. Yang, J. D. Chesko, and A. G. Suits, J. Chem. Phys. **102**, 6067 (1995).
[18] R. Toumi, P. L. Houston, and A. M. Wodtke, J. Chem. Phys. **104**, 775 (1996).
[19] P. L. Houston, A. G. Suits, and R. Toumi, J. Geophys. Res. **101**, 18829 (1996).

[20] C. A. Rogaski, J. M. Price, J. A. Mack, and A. M. Wodtke, Geophys. Res. Lett. **20**, 2885 (1993).
[21] C. A. Rogaski, J. A. Mack, and A. M. Wodtke, Faraday Discuss. **100**, 229 (1995).
[22] A. J. C. Varandas and A. A. C. C. Pais, in *Theoretical and Computational Models for Organic Chemistry*, edited by S. J. Formosinho, I. G. Czismadia, and L. G. Arnaut (Kluwer, Dordrecht, 1991), p. 55.
[23] H. Szichman, A. J. C. Varandas, and M. Baer, Chem. Phys. Lett. **231**, 253 (1994).
[24] H. Szichman, A. J. C. Varandas, and M. Baer, J. Chem. Phys. **102**, 3474 (1995).
[25] N. Balakrishnan and G. D. Billing, Chem. Phys. Lett. **242**, 68 (1995).
[26] N. Balakrishnan and G. D. Billing, J. Chem. Phys. **104**, 9482 (1996).
[27] J. A. Mack, Y. Huang, A. M. Wodtke, and G. C. Schatz, J. Chem. Phys. **105**, 7495 (1996).
[28] R. Hernández, R. Toumi, and D. C. Clary, J. Chem. Phys. **102**, 9544 (1995).
[29] R. Hernández-Lamoneda, M. I. Hernández, E. Carmona-Novillo, J. Campos-Martínez, J. Echave, and D. C. Clary, Chem. Phys. Lett. **276**, 152 (1997).
[30] D. Lauvergnat and D. C. Clary, J. Chem. Phys. **108**, 3566 (1998).
[31] N. Balakrishnan, A. Dalgarno, and G. D. Billing, Chem. Phys. Lett. **288**, 657 (1998).
[32] A. J. C. Varandas and W. Wang, Chem. Phys. **215**, 167 (1997).
[33] W. Wang and A. J. C. Varandas, Chem. Phys. **236**, 181 (1998).
[34] J. Campos-Martinínez, E. Carmona-Novillo, J. Echave, M. I. Hernández, R. Hernández-Lamoneda, and J. Palma, Chem. Phys. Lett. **289**, 150 (1998).
[35] B.-Y. Chang, R. C. Hoetzlein, J. A. Mueller, J. D. Geiser, and P. L. Houston, Rev. Sci. Instrum. **69**, 1665 (1998).
[36] D. J. Bamford, L. E. Jusinski, and W. K. Bischel, Phys. Rev. A **34**, 185 (1986).
[37] D. J. Bamford, M. J. Dyer, and W. K. Bischel, Phys. Rev. A **36**, 3497 (1987).
[38] A. T. J. B. Eppink and D. H. Parker, Rev. Sci. Instrum. **68**, 3477 (1997).
[39] L. A. Shepp and B. F. Logan, IEEE Trans. Nucl. Sci. **NS-21**, 21 (1974).
[40] L. Montgomery Smith and D. R. Keefer, J. Quant. Spectrosc. Radiat. Transf. **39**, 367 (1988).
[41] M. Kalal and K. A. Nugent, Appl. Opt. **27**, 1956 (1988).
[42] K. Takahashi, M. Kishigami, N. Taniguchi, Y. Matsumi, and M. Kawasaki, J. Chem. Phys. **106**, 6390 (1997).
[43] R. R. Laher and F. R. Gilmore, J. Phys. Chem. Ref. Data **20**, 685 (1991).
[44] C. E. Moore, *Tables of Spectra of Hydrogen, Carbon, Nitrogen, and Oxygen Atoms and Ions* (CRC, Boca Raton, 1993).
[45] K. Takahashi, N. Taniguchi, Y. Matsumi, and M. Kawasaki, Chem. Phys. **231**, 171 (1998).
[46] T. Kinugawa, T. Sato, T. Arikawa, Y. Matsumi, and M. Kawasaki, J. Chem. Phys. **93**, 3289 (1990).
[47] J. H. Seinfeld and S. N. Pandis, *Atmospheric Chemistry and Physics: From Air Pollution to Climate Change* (Wiley, New York, 1998).
[48] P. O'Keeffe, T. Ridley, S. Wang, K. P. Lawley, and R. Donovan, Chem. Phys. Lett. **298**, 368 (1998).
[49] R. Ogorzalek Loo, W. J. Marinelli, P. L. Houston, S. Arepalli, J. R. Wiesenfeld, and R. W. Field, J. Chem. Phys. **91**, 5185 (1989).
[50] D. R. Snelling and M. Gauthier, Chem. Phys. Lett. **9**, 254 (1971).
[51] L. T. Molina and M. J. Molina, J. Geophys. Res. **91**, 14501 (1986).
[52] S. M. Shamsuddin, Y. Inagaki, Y. Matsumi, and M. Kawasaki, Can. J. Chem. **72**, 637 (1994).
[53] R. T. Jongma, S. Shi, and A. M. Wodtke, J. Chem. Phys. (to be published).